Title

Interface control of bulk ferroelectric polarization

Journal

Proceedings of the National Academy of Sciences of the United States of America, 109(25)

ISSN

0027-8424

Authors

Yu, P
Luo, W
Yi, D
et al.

Publication Date

2012-06-19

DOI

10.1073/pnas.1117990109

Peer reviewed

Interface control of bulk ferroelectric polarization

P. Yu[a,1], W. Luo[b,c], D. Yi[a], J. X. Zhang[a], M. D. Rossell[d,e], C.-H. Yang[f], L. You[g], G. Singh-Bhalla[a,h], S. Y. Yang[a], Q. He[a], Q. M. Ramasse[d,i], R. Erni[d,j], L. W. Martin[k], Y. H. Chu[l], S. T. Pantelides[b,c], S. J. Pennycook[b,c], and R. Ramesh[a,h]

[a]Department of Physics and Department of Materials Science and Engineering, University of California, Berkeley, CA 94720; [b]Materials Science and Technology Division, Oak Ridge National Laboratory, Oak Ridge, TN 37831; [c]Department of Physics and Astronomy, Vanderbilt University, Nashville, TN 37235; [d]National Center for Electron Microscopy, Lawrence Berkeley National Laboratory, Berkeley, CA 94720; [e]Department of Materials, Eidgenössiche Technische Hochschule Zürich, CH-8093 Zürich, Switzerland; [f]Department of Physics, Institute for NanoCentury, Korea Advanced Institute of Science and Technology, Daejeon 305-701, Korea; [g]Department of Electrical Engineering and Computer Science, University of California, Berkeley, CA 94720; [h]Materials Sciences Division, Lawrence Berkeley National Laboratory, Berkeley, CA 94720; [i]SuperSTEM Laboratory, Science and Technology Facilities Council, Daresbury, Keckwick Lane, Daresbury WA4 4AD, England; [j]Empa, Swiss Federal Laboratories for Materials Science and Technology, CH-8600 Dübendorf, Switzerland; [k]Department of Materials Science and Engineering, University of Illinois at Urbana-Champaign, Urbana, IL 61801; and [l]Department of Materials Science and Engineering, National Chiao Tung University, Hsinchu 30010, Taiwan

Edited by Malcolm R. Beasley, Stanford University, Stanford, CA, and approved April 3, 2012 (received for review November 1, 2011)

The control of material interfaces at the atomic level has led to novel interfacial properties and functionalities. In particular, the study of polar discontinuities at interfaces between complex oxides lies at the frontier of modern condensed matter research. Here we employ a combination of experimental measurements and theoretical calculations to demonstrate the control of a bulk property, namely ferroelectric polarization, of a heteroepitaxial bilayer by precise atomic-scale interface engineering. More specifically, the control is achieved by exploiting the interfacial valence mismatch to influence the electrostatic potential step across the interface, which manifests itself as the biased-voltage in ferroelectric hysteresis loops and determines the ferroelectric state. A broad study of diverse systems comprising different ferroelectrics and conducting perovskite underlayers extends the generality of this phenomenon.

complex oxide | heterostructure | interface physics | electronic reconstruction | polar discontinuity

Over the past few years, precisely constructed, atomically sharp perovskite oxide heterointerfaces have become focal points for condensed-matter-physics and materials science research (1–5). The incorporation and reconstruction of spin (6, 7), charge (8–10), and orbital (11) degrees of freedom across the heterointerfaces have led to novel electronic properties that are different from those inherent to the individual components. For example, pioneering work on the $LaAlO_3$ and $SrTiO_3$ (STO) heterostructures has revealed a nontrivial two-dimensional electron gas (2DEG) (10, 12, 13) at the interface, which also exhibits magnetic (14) and even superconductivity properties (15) that are induced by the polar discontinuity (16) (valence mismatch) across the interface.

Motivated by this, research nowadays is primarily focused on probing and understanding the novel interfacial phenomena observed in complex-oxide heterostructures. However, the focus on interfacial properties sidesteps possible macroscopic implications of the interfacial atomic-scale control on the broad range of properties that are present in bulk complex oxides. On the other hand, in the semiconductor industry, atomic-scale interface engineering has long been used to improve the performance of devices through control of the threshold voltage (17), channel carrier mobility (18), Schottky barrier height (19), and so on. This forms the fundamental premise for this work: Can we control the bulk properties of a heterostructured system through the emergent state of matter at the interface? Such an approach could be particularly intriguing if one of the layers is highly polar and electrically switchable, i.e., ferroelectric in nature. Because functional ferroelectric systems, such as the nonvolatile memory (20), ferroelectric field effect transistor (21, 22), ferroelectric tunnel junction (23–27), and switching photo-diode (28), are strongly correlated with the interface electronic structures, it is of great importance to study how the interface atomic engineering can be employed to control the ferroelectric polarization state. Based on this premise, we describe a model experiment in which the polarization state of a ferroelectric layer was directly controlled through the interfacial chemical termination. Our observations indicate a strong, delocalized interface effect with important implications for future electronics based on such materials.

We begin by exploring the ferroelectric perovskite $BiFeO_3$ (BFO) and conducting manganite $La_{0.7}Sr_{0.3}MnO_3$ (LSMO) heterostructure as our model interface, in which numerous novel coupling phenomena related with the spin (29, 30) and lattice (31) degrees of freedom have been unveiled by previous studies. Here we explore another interesting coupling behavior across such an interface: how the inherent interface valence mismatch can influence the ferroelectric states of a BFO layer grown on an LSMO bottom electrode. Through the use of reflection high-energy electron diffraction (RHEED)-assisted pulsed laser deposition, the interface between LSMO and BFO can be precisely engineered with atomic-scale sharpness. Subsequent investigations of ferroelectric order indicate that the as-grown polarization direction is determined by the interface termination and its fine level control of the interface electrostatic potential.

The key to controlling the ferroelectric polarization direction in the BFO epilayer lies in the ABO_3 perovskite structure exhibited by both LSMO and BFO, which enables two different kinds of interfaces to be created in [001]-oriented heterostructures. If the LSMO layer is terminated at the MnO_2-plane, we can effectively create an interface with the stacking sequence of $La_{0.7}Sr_{0.3}O$- (MnO_2)-BiO-FeO_2 (MnO_2-terminated interface) (Fig. 1*A*). On the other hand, if the LSMO layer is terminated at the $La_{0.7}Sr_{0.3}O$-plane, the stacking sequence changes to MnO_2-$(La_{0.7}Sr_{0.3}O)$-FeO_2-BiO ($La_{0.7}Sr_{0.3}O$-terminated interface) (Fig. 1*B*). Such atomically precise termination control can be achieved by utilizing TiO_2-terminated STO (001) substrates obtained with etch/thermal anneal procedures (32). The MnO_2-terminated LSMO was grown by direct, RHEED-controlled deposition of 13 unit cells of LSMO on the TiO_2-terminated STO substrate. During the growth of LSMO, clear intensity oscillations of the specular reflection spot can be observed (Fig. 1*C*), indicating a layer-by-layer growth mode. For the growth of $La_{0.7}Sr_{0.3}O$-terminated LSMO film, we first need to modify the STO substrate from TiO_2 termination to SrO termination. To achieve this, a very thin layer (2.5 unit cells) of $SrRuO_3$ was grown on STO.

Author contributions: P.Y., Y.-H.C., and R.R. designed research; P.Y., W.L., D.Y., J.X.Z., M.D.R., C.-H.Y., L.Y., S.-Y.Y., Q.H., Q.M.R., R.E., and L.W.M. performed research; P.Y., W.L., M.D.R., and C.-H.Y. analyzed data; and P.Y., W.L., M.D.R., G.S.-B., L.W.M., Y.-H.C., S.T.P., S.J.P., and R.R. wrote the paper.

The authors declare no conflict of interest.

This article is a PNAS Direct Submission.

Freely available online through the PNAS open access option.

[1]To whom correspondence should be addressed. E-mail: yupu.phy@gmail.com.

This article contains supporting information online at www.pnas.org/lookup/suppl/doi:10.1073/pnas.1117990109/-/DCSupplemental.

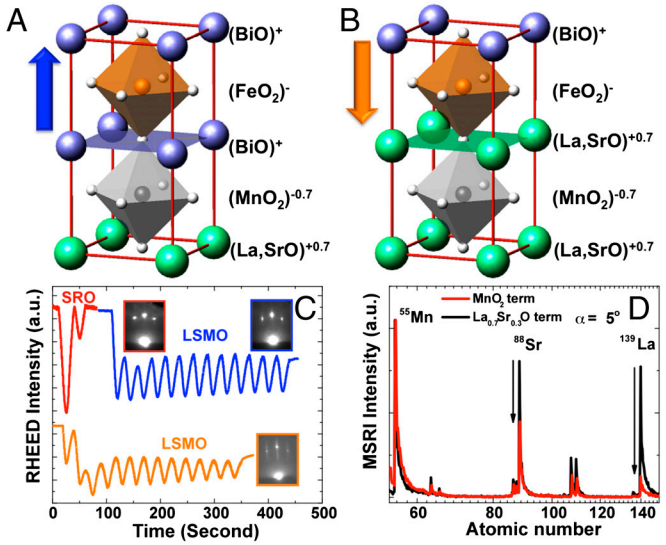

Fig. 1. Schematic model and experimental design of two possible heterointerfaces between LSMO and BFO layers. Schematics of atomic stacking sequence for LSMO/BFO heterostructures with $La_{0.7}Sr_{0.3}O$-MnO_2-BiO-FeO_2 (*A*) and MnO_2-$La_{0.7}Sr_{0.3}O$-FeO_2-BiO (*B*) interfaces. The sheet charge density for each layer has been assigned following the nominal bulk valence. The arrows indicate the as-grown directions of the ferroelectric polarizations in BFO layers. (*C*) RHEED intensity oscillations of the specular reflected beam during the growth of $SrRuO_3$ and $La_{0.7}Sr_{0.3}MnO_3$ on the TiO_2-terminated $SrTiO_3$ (001) surface. (*D*) TOF-ISARS spectra of MnO_2- and $La_{0.7}Sr_{0.3}O$-terminated $La_{0.7}Sr_{0.3}MnO_3$ thin films.

Because the RuO_2-layer is highly volatile, this material will be self-terminated with SrO surface (33), which leads to the half-integral unit cell growth (Fig. 1*C*) as well as change of termination from TiO_2 to SrO. This approach could also be realized with the growth of one monolayer of SrO on the TiO_2 terminated STO substrates (Fig. S1). Subsequent deposition of 13 unit cells of LSMO on this surface results in a $La_{0.7}Sr_{0.3}O$-terminated layer. For both structures, topography images taken by atomic force microscopy (AFM) (*SI Text* and Fig. S2) show the presence of atomically flat terraces as defined by the underlying vicinal substrate and separated by steps of height approximately 4 Å, which imply the single termination on these samples.

To confirm that our controlled growth protocol indeed leads to different terminations of LSMO layers, time-of-flight ion scattering and recoil spectroscopy (TOF-ISARS) (34) was used to characterize surface chemistries (details are described in *Materials and Methods*, *SI Text*, and Fig. S3). TOF-ISARS is a nondestructive, real-time probe capable of providing direct information on surface composition and atomic structure of the first few monolayers (35, 36). Fig. 1*D* shows the mass spectroscopy of recoiled ions (MSRI), normalized to the ^{55}Mn peak, for the two different surface terminations. The results reveal that the LSMO films grown on thin SRO buffer layers exhibit strongly enhanced La- and Sr-peak intensities, which suggests that the surface composition of the films is indeed La- and Sr-rich, consistent with the nominal $La_{0.7}Sr_{0.3}O$-layer termination. In contrast, the LSMO films grown directly on the TiO_2-terminated STO substrates show relatively lower intensities of the La- and Sr-peaks, suggesting MnO_2-layer termination. These results together with the AFM images indicate that we can indeed control the surface termination of the LMSO layers through the growth protocol described above.

To shed light on the interfacial atomic structure of the LSMO/BFO heterostructure and complement the macroscopic TOF-ISARS measurements, high-resolution scanning transmission electron microscopy (STEM) imaging and atomic-scale electron energy-loss spectroscopy (EELS) analysis (details of measurements are provided in *Materials and Methods*) have been carried out and are shown in Fig. 2. The cross-section STEM imaging (Fig. 2 *A* and *B*, *SI Text*, and Fig. S4) illustrates the layered architecture of the heterostructures and suggests the presence of atomically abrupt epitaxial interfaces between the LSMO and BFO layers. Fig. 2 *C* and *D* depict the integrated EELS signals of the Fe $L_{3,2}$, Mn $L_{3,2}$, and La $M_{5,4}$ absorption edges, simultaneously recorded along a line as displayed in the corresponding STEM images (Fig. 2 *A* and *B*). The characteristics of the Fe, Mn, and the La signals reflect the expected atomic structure within the LSMO and the BFO layers, and the modulations of the individual EELS signals at the interface suggest sharp chemical profiles in the interface plane. Combining the information from the EELS studies, the high-angle annular dark field (HAADF) intensity profiles, and the HAADF-STEM images, the interface atomic configurations can be deduced to be $La_{0.7}Sr_{0.3}O$-MnO_2-BiO-FeO_2 (Fig. 2 *A* and *C*) and MnO_2-$La_{0.7}Sr_{0.3}O$-FeO_2-BiO (Fig. 2 *B* and *D*), respectively. Thus, we are confident that the interface between LSMO/BFO in such artificial heterostructures can be engineered to exhibit two different interface terminations, which provides a solid platform to trigger the study of emergent coupling phenomena at these oxide interfaces.

We proceeded to examine how these different interfacial structures impact the nature of the electronic interactions at these heterointerfaces. Piezoresponse force microscopy (PFM) (37) was employed to study the polarization state of the ferroelectric BFO layers (Fig. 3 *A* and *B*). The contrast of the out-of-plane PFM image is correlated with the orientation of the ferroelectric polarization, with the dark (bright) region indicating upward (downward) ferroelectric polarization. Strikingly, the as-grown polarization direction is directly correlated with the interface termination of the heterostructure. For samples possessing the MnO_2-terminated interface, the as-grown state is upward (pointing from the bottom electrode to the top surface) (Fig. 3*A*). On the

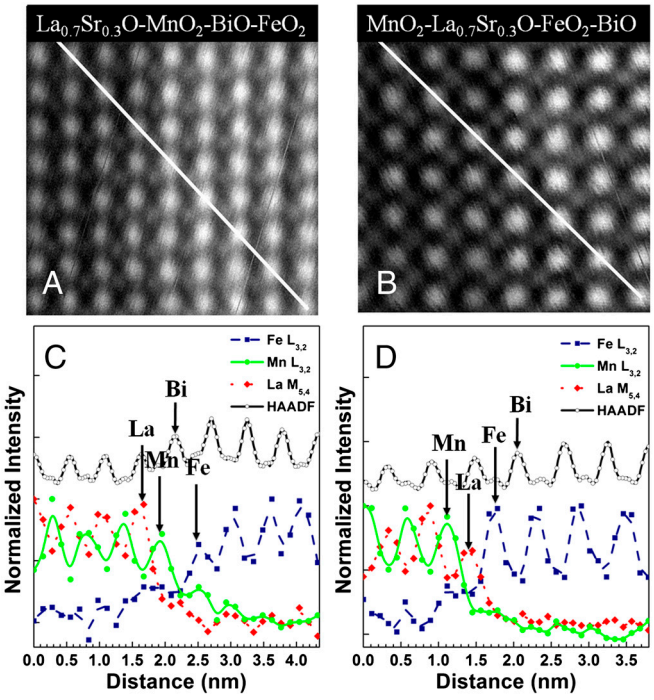

Fig. 2. Atomic-scale structure and chemical characterization of LSMO/BFO heterointerfaces. High-resolution HAADF-STEM images of heterostructures with the $La_{0.7}Sr_{0.3}O$-MnO_2-BiO-FeO_2 (*A*) and MnO_2-$La_{0.7}Sr_{0.3}O$-FeO_2-BiO (*B*) interfaces, and the corresponding chemical profiles across the respective interfaces (*C* and *D*). The EELS line scans are acquired diagonally from the top left to the bottom right of the HAADF images (indicated with a white line).

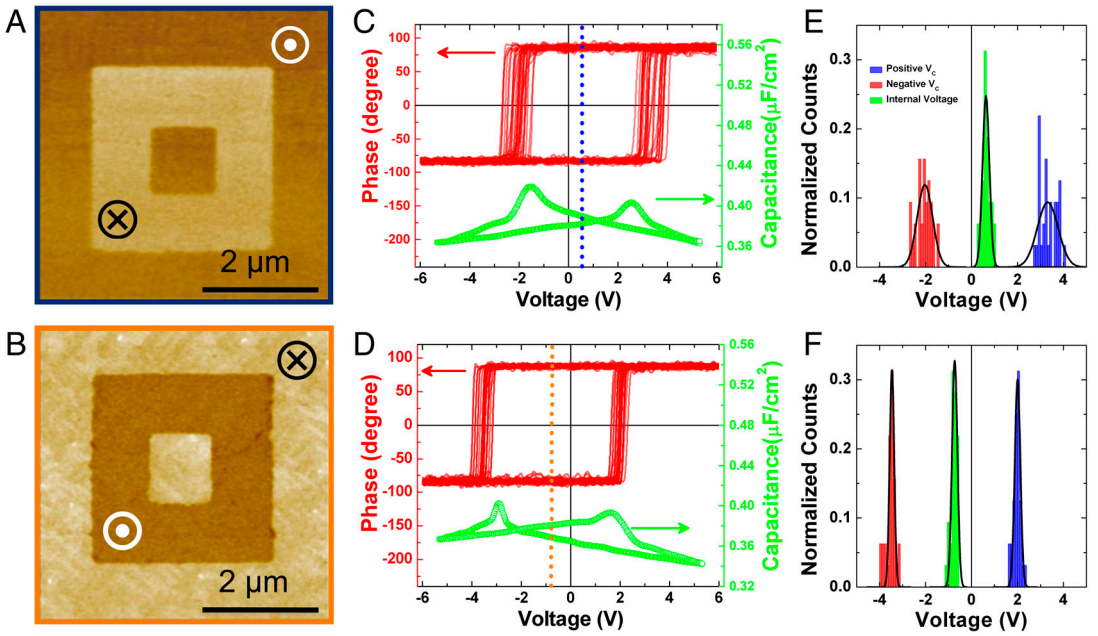

Fig. 3. Ferroelectric polarization switching. Typical out-of-plane PFM images of as-grown LSMO/BFO heterostructures with $La_{0.7}Sr_{0.3}O$-MnO_2-BiO-FeO_2 (*A*) and MnO_2-$La_{0.7}Sr_{0.3}O$-FeO_2-BiO (*B*) interfaces, and corresponding typical quasistatic piezoresponse (*Top*, red) and capacitance-voltage (*Bottom*, green) hysteresis loops (*C* and *D*). The samples used in the study are 150 nm BFO thin films with 5 nm LSMO bottom electrodes. The top electrodes used are 100 nm Au with 30 microns square. The consistent shift of the loops indicates the presence of a biased-voltage due to the electrical mismatch between the bottom (conducting layer) and top (Au) electrodes. (*E* and *F*) Histogram analysis of the obtained coercive voltages (red and blue) and biased-voltages (green) from the piezoresponse measurements present in *C* and *D*. The solid lines show best Gaussian fits for the data.

contrary, the as-grown state is exactly opposite (downward) for samples possessing the $La_{0.7}Sr_{0.3}O$-terminated interface (Fig. 3*B*). We have also probed the ferroelectric nature of these films via local switching studies using PFM tips. The sharp contrast between the opposite polarizations in the PFM images (Fig. 3 *A* and *B*) as well as the presence of square hysteresis loops in the piezoelectric (or ferroelectric) switching (Fig. 3 *C* and *D*) strongly indicates that these films are of very high quality and possess good ferroelectric properties.

To elucidate the relationship between the interface termination and ferroelectric polarization of the heterostructure, first-principles density-functional-theory (DFT) calculations (38) have been carried out (see *Materials and Methods* for details). The Fig. 4*A*, *Top*, shows a schematic of the supercell used in the calculations, in which the chemical compositions of the two interfaces between BFO and LSMO layers are set up to be asymmetric, i.e., one is MnO_2- and the other is $La_{0.5}Sr_{0.5}O$-terminated. The calculations show that the total energy of the system is lower (1.13 eV for the whole supercell) when the [001] component of ferroelectric polarization in BFO points from MnO_2- to $La_{0.5}Sr_{0.5}O$-terminated interface. This calculated preferred direction of ferroelectric polarization is consistent with the measured as-grown states of MnO_2- and $La_{0.7}Sr_{0.3}O_2$-terminated BFO films.

To trace the origin of the preference of the ferroelectric polarization, the macroscopic averages of the atomic-scale electrostatic potentials (39) across the two inequivalent interfaces have been calculated and are shown in Fig. 4*A*. When the ferroelectric polarization is against the preferred direction ("P Left"), a large potential gradient is formed, counteracting the ferroelectric polarization across the BFO layer and resulting in the enhancement of the depolarization field. On the contrary, the potential gradient is much reduced when the ferroelectric polarization is in the preferred direction ("P Right"). These results are consistent with the lower total energy.

We note that the observed potential gradient is due to the superposition of several factors, of which the two most important are illustrated in the top two panels of Fig. 4*B*. The first one is the ferroelectric depolarization field. Fig. 4*B*, *Top*, illustrates the potential profiles from the ferroelectric depolarization field

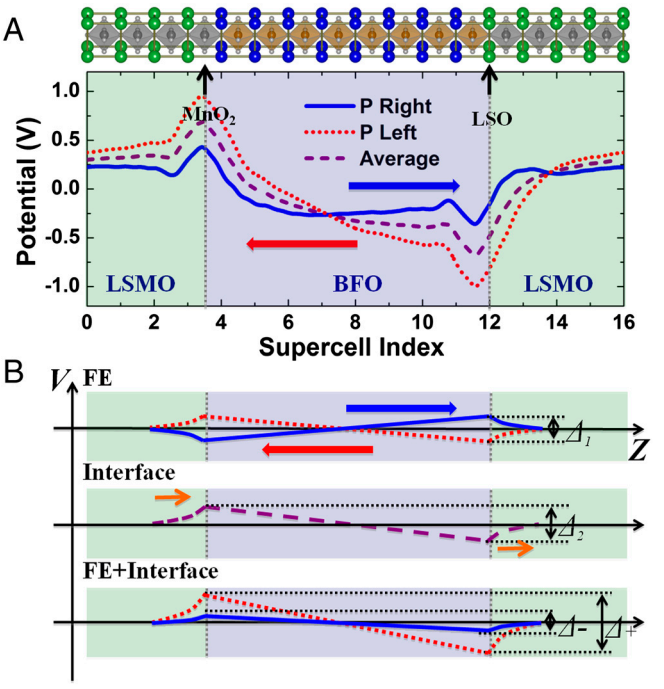

Fig. 4. First-principles calculations and schematic illustrations of electronic reconstruction across LSMO/BFO heterointerfaces. (*A*) Macroscopic averages of the electrostatic potentials for the two inequivalent ferroelectric polarization directions and their average. A schematic of the supercell used in the study is displayed in the top panel. (*B*) Schematic illustration of the electrostatic potential through the supercell due to the contribution of ferroelectric depolarization field (*Top*), the asymmetric interfaces (*Middle*), and the combination of both (*Bottom*). The red and blue arrows indicate the ferroelectric polarization directions, and the orange arrows illustrate the interface dipole due to the valence mismatch.

of a sandwich structure, in which a potential step (Δ_1) is built up across the ferroelectric material, with the electric field direction antiparallel to the ferroelectric polarization. The second one is the electrostatic difference between the two inequivalent interfaces, which is responsible for the observed preference of the ferroelectric polarization directions (Fig. 4*B*, *Middle*). We note that the first contribution switches sign as the polarization is reversed. Thus the average of the electrostatic potentials for two opposite polarization configurations (purple dashed curve in Fig. 4) is a good estimation of the intrinsic electrostatic potential difference resulting from the interface valence mismatch, in which approximately a potential step of 1.3 V forms between the two asymmetric interfaces.

This calculated result is also understandable based on the so-called polar discontinuity (valence mismatch) model (10, 16). Although this model was first proposed to study the interface between insulating materials, recently there has been growing interest to adapt it as well for the study of the interface between conducting and insulating materials. Because the charge transfer along the perpendicular direction of the interface is highly inhibited by the adjacent insulator layer, it is still reasonable to assume the layer valence state at the interface of this conducting material. Indeed this model has been successfully employed to the study of LSMO/STO interface (7, 40–43).

Within the framework of the polar discontinuity model (10, 16), the sheet charge density at the MnO_2-terminated interface (Fig. 1*A*) is assigned to be $+0.7e/-0.7e/+1e/-1e$, which results in a nominal positive charge of $+0.15e$ ($0.7/2-0.7+1/2=0.15$) at the interface and eventually leads to an interface dipole pointing from the LSMO layer to the interface (Fig. 4*B*, *Middle*) due to the Thomas Fermi screening (40, 41). Similarly, an interface dipole pointing from the interface to the LSMO layer is associated with the $La_{0.7}Sr_{0.3}O$-terminated interface due to a nominal negative interface charge of $-0.15e$ (Fig. 1*B*). As a consequence, a potential step (Δ_2) forms across the heterostructure as shown in the middle panel of Fig. 4*C*, and the sign of which is in agreement with our calculations (Fig. 4*A*). Furthermore, the combination of these two mechanisms (Fig. 4*B*, *Bottom*) reproduces in a schematic way the DFT results (Fig. 4*A*).

Experimentally, the magnitude of the interface-induced electrostatic potential step can be estimated quantitatively from the piezoresponse (or ferroelectric) hysteresis measurements (Fig. 3 *C* and *D*). Due to the difference in the work functions of the bottom and the top electrodes, the hysteresis loop is typically asymmetric about the voltage axis, with a biased-voltage of $V_{\text{int}}=(V_{+}+V_{-})/2$ (20), where V_{+} and V_{-} are the positive and negative coercive voltages, respectively. In our study, the phase loops were used to determine the coercive voltages, because it shows sharper transitions between different polarization states when compared with the amplitude loops. To achieve reliable statistics, we have carried out multimeasurements (approximately 32) on both heterostructures, with the measured coercive and biased voltages summarized in the histograms shown in Fig. 3 *E* and *F*. As these data show, for both interface configurations, the biased-voltage distributions have similar Gaussian profiles, and the biased-voltages were determined to be 0.63 ± 0.18 and -0.72 ± 0.14 V for the heterostructure with MnO_2- and $La_{0.7}Sr_{0.3}O$-terminated interfaces, respectively. Because the top electrodes (Au) used for the measurements of both terminations are the same, the difference between the biased-voltages is taken as a measure of the induced interface electrostatic potential step. The observed difference of approximately 1.35 V is in agreement with the results obtained by first-principles DFT calculations. This finding is also in line with the recent studies of the STO and LSMO heterointerface (40–42), in which a potential step is formed across the interface due to the valence mismatch. Furthermore, we have also carried out quasistatic capacitance-voltage measurements on both interface configurations and compared with piezoresponse hysteresis measurements (Fig. 3 *C* and *D*). Notably, both these quasistatic measurement techniques consistently reveal the presence of a biased-voltage in their respective loops. It is worth noting that the biased-voltages can also be obtained and spatially mapped by using a PFM tip as top contact (44, 45). Indeed, we have obtained consistent interface-induced electrostatic potential steps by using both the Au pads and PFM tips as top contacts (Fig. S5).

To shed more light on this approach, we have also carried out both the thickness dependent (Fig. 5*A*) and dynamic analysis (Fig. 5*B*) of these interface-induced electrostatic potential steps. First, we have measured the as-grown ferroelectric polarization states and piezoresponse hysteresis loops for BFO films with thickness in the range of 10 to 150 nm. The consistent as-grown polarization directions (Fig. S6) as well as biased-voltages (Fig. 5*A*) through the whole thickness range strongly suggest that the effect observed is directly correlated with the interface atomic stacking sequences, but not the film thickness. Furthermore, frequency dependent measurements of the ferroelectric polarization hysteresis loop for BFO thin films were performed and are presented in Fig. 5*B*. These measurements have been done with exactly the same structures as shown in Fig. 3 *C* and *D*. For both interface configurations, we observed a shift of hysteresis loops along the voltage axis (Fig. S7), being consistent with the quasistatic piezoresponse and capacitance-voltage measurements. Careful analysis further reveals that the coercive-voltages show clear frequency dependence, which can be fitted to an empirical relationship based on the Kolmogorov–Avrami–Ishibashi (KAI) theory (46, 47) (Fig. S7). On the other hand, the biased-voltages are almost constant in the frequency range from 0.02 Hz to 10 kHz (Fig. 5*B*), highlighting the fact that this effect is not related with the ferroelectric switching or any other dynamic process.

Finally, the generality of this experimental approach has been further extended to other ferroelectrics and conducting oxides listed in Table 1 (Fig. S1 and Figs. S8–S11 for growth and experimental details, respectively). Despite the variable carrier type, carrier density, and work function of the electrodes, the PFM studies reveal exclusively that the ferroelectric polarization is controlled by the interface valence mismatch. Careful inspection of the local ferroelectric hysteresis loops (with PFM tips as top contacts) confirms the generality of the finding that an induced electrostatic potential step is formed as a consequence of the interface valence mismatch, which controls the polarization state of the ferroelectric.

In summary, we have demonstrated that atomically precise control of the interface can lead to dramatically different polar states in ferroelectrics. This occurs primarily through the coupling

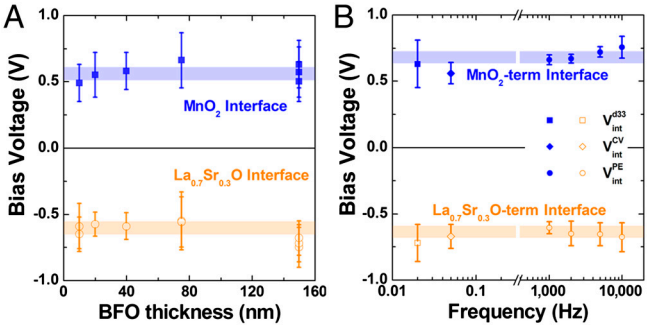

Fig. 5. Thickness and frequency dependent measurements of biased-voltages across LSMO/BFO heterointerfaces. (*A*) BFO thickness dependence of bias-voltages for BFO/LSMO heterostructures with both interface configurations. The bias-voltages were obtained with piezoresponse measurements. (*B*) Frequency dependent analysis biased-voltages of 150 nm BFO obtained from various measurement techniques. The frequencies of piezoresponse (d_{33}) and CV measurements were set to 0.02 and 0.05 Hz based on the total measurement time of about 50 and 20 s, respectively.

Table 1. Electronic reconstruction across the polar interfaces of ferroelectric heterostructures

Structure	Electrode termination	Valence mismatch	Polarization state	Internal field (V)	Electrostatic potential step (V)
BFO/LSMO	A site	−0.3	Down	−0.55 ± 0.22	1.2 ± 0.3
	B site	+0.3	Up	0.66 ± 0.21	
BFO/SRO	A site	−1.0	Down	−0.75 ± 0.18	1.5 ± 0.3
	B site	+1.0	Up	0.79 ± 0.20	
BFO/Nb:STO	A site	−1.0	Down	−1.2 ± 0.3	2.6 ± 0.4
	B site	+1.0	Up	1.4 ± 0.3	
PZT/LSMO	A site	+0.7	Up	0.86 ± 0.32	1.6 ± 0.4
	B site	−0.7	Down	−0.72 ± 0.25	

The valence mismatch at the interface is calculated by assuming the ionic charge assignment with the nominal bulk valence for each layer. For example, the MnO_2-terminated ($La_{0.7}Sr_{0.3}O$-MnO_2-BiO-FeO_2) interface has the sheet charge density as $+0.7e/-0.7e/+1e/-1e$; thus the valence mismatch is calculated to be $-0.7+1=0.3$. The interface electrostatic potential step is calculated to be the difference between the biased-voltages of the two possible interface configurations within the same structure. The data on LSMO/BFO heterostructures were obtained from the piezoresponse measurements with Au as top electrodes; all the other heterostructures were measured with PFM tips as top contacts. The B site-terminated SRO is achieved by depositing an atomic layer of TiO_2 on top of SrO-terminated SRO.

of the interface electrostatic potential step to the polar order. We note that whereas there is considerable interest in the scientific community focused on the interface itself (and various phenomena related to the interface), we argue that the influence on the bulk properties of the thin films can be equally important. We hope this paper draws attention to this heretofore-unexplored possibility.

Materials and Methods

Film Growth. Thin films were grown by pulsed laser deposition while utilizing high-pressure RHEED to verify the growth mechanism. Growth was performed on $SrTiO_3$ (001) (STO) single crystal substrates, which provides good lattice matching for the various heterostructures. Before the growth, a buffered HF acid-etch and thermal treatment process was used to obtain fully TiO_2 (B site)-terminated surfaces (32). Atomic force microscopy (AFM) measurements reveal perfect one unit-cell-height surface steps and terraces. The SRO layer was grown at 650 °C in 100 mTorr of oxygen pressure. Both the LSMO and BFO layers were grown at 690 °C in 150 mTorr of oxygen pressure. The PZT layer was grown at 630 °C in 100 mTorr of oxygen pressure. The *AO* (SrO) -terminated Nb: STO was achieved by depositing one monolayer of SrO on top of treated BO_2 (TiO_2) -terminated Nb: STO substrate. Using a single crystal target, SrO was grown at a heater temperature of 500 °C under an oxygen ambient of 1 mTorr. Similarly, the BO_2-terminated SRO was achieved by depositing one monolayer of TiO_2 on top of *AO* (SrO) -terminated SRO. The TiO_2 atomic layer was grown at a heater temperature of 700 °C under an oxygen ambient of 10 mTorr. The laser energy was fixed at 1.5 mJ/cm^2 for all of the materials. After the growth, the samples were cooled to room temperature under an oxygen ambient of 760 Torr at a rate of 5 °C/ min. Post-annealing process has been carried out at 400 °C under an oxygen ambient for 1 h to ensure samples were fully oxidized.

Time-of-Flight Ion Scattering and Recoiled Ion Spectroscopy (TOF-ISARS). Time-of-flight ion scattering and recoiled ion spectroscopy (TOF-ISARS) uses the mass-to-charge ratio of the recoil ions to identify the chemical composition at the sample surface. Pulsed potassium ions are accelerated to 10 keV and directed toward the film surface to produce recoiled ions from the sample at an incident angle of 5° or 15°, and the MSRI are measured at a recoil angle of 60°. For small grazing incidence angles (approximately 5°), this technique is extremely surface sensitive and yields dramatically different signal intensity between compositions of the first and the second monolayer. In this measurement, the LSMO samples with both MnO_2- and $La_{0.7}Sr_{0.3}O$-terminated layers were prepared by the process described above and then transferred to the TOF-ISARS chamber, which has a base pressure of 10^{-8} Torr. Prior to the measurement, the samples were heated to 650 °C in an oxygen pressure of 100 mTorr for 1 h to remove any hydrocarbon contaminants and organic residues from the surface. The measurements were carried out at room temperature after this thermal annealing process. The small peaks around an atomic number of 108 correspond to silver isotopes stemming from the silver paint used for making thermal contact of the sample to the heater block and does not affect the conclusion about the surface termination.

Transmission Electron Microscopy. HAADF-STEM was carried out using the TEAM 0.5 microscope (48) (a modified FEI Titan 80–300 equipped with CEOS aberration corrector) operated at 300 kV, and the corrected VG Microscopes HB 501 dedicated STEM (equipped with Nion aberration corrector), both located at the National Center for Electron Microscopy (NCEM). All EELS was carried out on an aberration-corrected VG HB 501, equipped with a Gatan Enfina spectrometer and operating at a voltage of 100 kV. In typical operating conditions for the experiments, the microscope provides an estimated spatial resolution of 0.12 nm, simultaneously with a 0.5 eV energy resolution in EELS, as shown in Fig. 2. For all imaging and spectroscopy work, the probe semiconvergence angle was 21 mrad, while the EELS spectra were collected through an 18-mrad semiaperture angle; the annular semidetection range was calibrated at 72–210 mrad for the HAADF detector.

Ferroelectric Measurements. Piezoresponse force microscopy measurement was carried out with an AFM-based setup (Veeco-DI equipped with a Nanoscope IV controller) under ambient conditions using a commercially Ti/Pt-coated Si tip (MikroMasch). The images were acquired in contact mode with a driving voltage of 3 V peak-to-peak at 6.39 kHz and a scanning rate of 1 μm/s. With the same setup, piezoelectric hysteresis loops were characterized by recording the surface displacement as a function of applied DC voltage (up to ±8 V), with a driving voltage of 0.5 V at 6.39 kHz applied to the AFM tip. Ferroelectric polarization hysteresis loops and ferroelectric measurements were performed using a RT6000 test system (Radiant Technologies). Capacitance-voltage hysteresis loops were measured using impedance analyzer (HP 4194A). For all the measurements, the biased electric field is applied though the top electrodes, while the bottom electrodes (LSMO) are grounded.

First-Principles Calculations. First-principles density-functional theory calculations were performed using the projector augmented-wave method and the VASP code (38). The spin-polarized generalized-gradient approximation was used for the exchange-correlation functional. We used a supercell constructed from 8 LSMO and 8 BFO unit cells stacked along the pseudocubic [001] direction, so that the whole supercell contains $\sqrt{2}\times\sqrt{2}\times 16$ pseudocubic perovskite units. The two interfacial atomic planes between the FeO_2 and MnO_2 planes were chosen to be asymmetric, i.e., one interface is BiO and the other interface is $La_{0.5}Sr_{0.5}O$. The in-plane lattice constant was fixed to the substrate STO lattice constant of 3.905 Å, and the internal atomic positions in the supercell were optimized.

ACKNOWLEDMENTS. Research at Berkeley was sponsored by the Semiconductor Research Corporation-Nanoelectronics Research Initiative-Western Institute of Nanoelectrics program as well as by the Director, Office of Science, Office of Basic Energy Sciences, Materials Sciences and Engineering Division of the US Department of Energy under contract DE-AC02-05CH11231 (electron microscopy). The Materials Sciences and Engineering Division, Office of Basic Energy Sciences, US Department of Energy, supported work at Oak Ridge National Laboratory. Research at Vanderbilt was supportd by US Department of Energy Grant DE-FG02-09ER46554 and by the McMinn Endowment. C.-H.Y. acknowledges the support by the National Research Foundation of Korea funded by the Ministry of Education, Science and Technology (2010-0013528). L.W.M. acknowledges support from the Army Research Office under Grant W911NF-10-1-0482. Y.H.C. acknowledges the support from the National Science Council under contract 099-2811-M-009-003.

1. Heber J (2009) Materials science: Enter the oxides. *Nature* 459:28–30.
2. Mannhart J, Schlom DG (2010) Oxide interfaces—an opportunity for electronics. *Science* 327:1607–1611.
3. Zubko P, et al. (2011) Interface physics in complex oxide heterostructures. *Annu Rev Condens Matter Phys* 2:141–165.
4. Hwang HY, et al. (2012) Emergent phenomena at oxide interfaces. *Nat Mater* 11:103–113.
5. Chakhalian J, Millis AJ, Rondinelli J (2012) Whither the oxide interface. *Nat Mater* 11:92–94.
6. Ueda K, Tabata H, Kawai T (1998) Ferromagnetism in LaFeO3-LaCrO3 superlattices. *Science* 280:1064–1066.
7. Yamada H, et al. (2004) Engineered interface of magnetic oxides. *Science* 305:646–648.
8. Ohtomo A, Muller DA, Grazul JL, Hwang HY (2002) Artificial charge-modulation in atomic-scale perovskite titanate superlattices. *Nature* 419:378–380.
9. Okamoto S, Millis AJ (2004) Electronic reconstruction at an interface between a Mott insulator and a band insulator. *Nature* 428:630–633.
10. Ohtomo A, Hwang HY (2004) A high-mobility electron gas at the $LaAlO_3/SrTiO_3$ heterointerface. *Nature* 427:423–426.
11. Chakhalian J, et al. (2007) Orbital reconstruction and covalent bonding at an oxide interface. *Science* 318:1114–1117.
12. Huijben M, et al. (2009) Structure property relation of $SrTiO_3/LaAlO_3$ interfaces. *Adv Mater* 21:1665–1677.
13. Chen H, Kolpak AM, Ismail-Beigi S (2010) Electronic and magnetic properties of $SrTiO_3/LaAlO_3$ interfaces from first principles. *Adv Mater* 22:2881–2899.
14. Brinkman A, et al. (2007) Magnetic effects at the interface between non-magnetic oxides. *Nat Mater* 6:493–496.
15. Reyren N, et al. (2007) Superconducting interfaces between insulating oxides. *Science* 317:1196–1199.
16. Nakagawa N, Hwang HY, Muller DA (2006) Why some interfaces cannot be sharp. *Nat Mater* 5:204–209.
17. Wilk GD, Wallace RM, Anthony JM (2001) High-k gate dielectrics: Current status and materials properties considerations. *J Appl Phys* 89:5243–5275.
18. Houssa M, et al. (2006) Electrical properties of high-k gate dielectrics: Challenges, current issues, and possible solutions. *Mater Sci Eng R* 51:37–85.
19. Capasso F, et al. (1985) Doping interface dipoles: Tunable heterojunctions barrier heights and band-edge discontinuities by molecular beam epitaxy. *Appl Phys Lett* 46:664–666.
20. Scott JF (2000) *Ferroelectric Memories* (Springer, Berlin).
21. Mathews S, et al. (1997) Ferroelectric field effect transistor based on epitaxial perovskite heterostructures. *Science* 276:238–240.
22. Ahn CH, et al. (1999) Electrostatic modulation of superconductivity in ultrathin $GdBa_2Cu_3O_{7-x}$ films. *Science* 284:1152–1155.
23. Tsymbal E, Kohlstedt H (2006) Tunneling across a ferroelectric. *Science* 313:181–183.
24. Gajek M, et al. (2007) Tunnel junctions with multiferroic barriers. *Nat Mater* 6:296–302.
25. Garcia V, et al. (2009) Giant tunnel electroresistance for non-destructive readout of ferroelectric states. *Nature* 460:81–84.
26. Maksymovych P, et al. (2009) Polarization control of electron tunneling into ferroelectric surfaces. *Science* 324:1421–1425.
27. Garcia V, et al. (2010) Ferroelectric control of spin polarization. *Science* 327:1106–1110.
28. Choi T, et al. (2009) Switchable ferroelectric diode and photovoltaic effect in BiFeO3. *Science* 324:63–66.
29. Yu P, et al. (2010) Interface ferromagnetism and orbital reconstruction in $BiFeO_3$-$La_{0.7}Sr_{0.3}MnO_3$. *Phys Rev Lett* 105:027201.
30. Wu SM, et al. (2010) Reversible electric control of exchange bias in a multiferroic field-effect device. *Nat Mater* 9:756–761.
31. Borisevich AY, et al. (2010) Suppression of octahedral tilts and associated changes in electronic properties at epitaxial oxide heterostructure interfaces. *Phys Rev Lett* 105:087204.
32. Kawasaki M, et al. (1994) Atomic control of the $SrTiO_3$ crystal surface. *Science* 266:1540–1542.
33. Rijnders G, Blank DHA, Choi J, Eom CB (2004) Enhanced surface diffusion through termination conversion during epitaxial $SrRuO_3$ growth. *Appl Phys Lett* 84:505–507.
34. Rabalais JW (2003) *Principles and Applications of Ion Scattering Spectroscopy* (Wiley, New Jersey).
35. Kleibeuker JE, et al. (2010) Atomically defined rare-earth scandate crystal surfaces. *Adv Funct Mater* 20:3490–3496.
36. Biswas A, et al. (2011) Universal Ti-rich termination of atomically flat $SrTiO_3$ (001), (110), and (111) surfaces. *Appl Phys Lett* 98:051904.
37. Zavaliche F, et al. (2006) Multiferroic $BiFeO_3$ films: Domain structure and polarization dynamics. *Phase Transit* 79:991–1017.
38. Kresse G, Furthmuller J (1996) Efficient iterative schemes for ab initio total-energy calculations using a plane-wave basis set. *Phys Rev B* 54:11169–11186.
39. Peressi M, Binggeli N, Baldereschi A (1998) Band engineering at interfaces: Theory and numerical experiments. *J Phys D* 31:1273–1299.
40. Hikita Y, Nishikawa M, Yajima T, Hwang HY (2009) Termination control of the interface dipole in $La_{0.7}Sr_{0.3}MnO_3$/Nb : $SrTiO_3$ (001) Schottky junctions. *Phys Rev B* 79:073101.
41. Burton JD, Tsymbal EY (2010) Evolution of the band alignment at polar oxide interfaces. *Phys Rev B* 82:161407(R).
42. Zheng B, Binggeli N (2010) Influence of the interface atomic structures on the magnetic and electronic properties of $La_{2/3}Sr_{1/3}MnO_3/SrTiO_3$ (001) heterojunctions. *Phys Rev B* 82:245311.
43. Yajima T, Hikita Y, Hwang HY (2011) A heteroepitaxial perovskite metal-base transistor. *Nat Mater* 10:198–201.
44. Jesse S, Baddorf AP, Kalinin SV (2006) Switching spectroscopy piezoresponse force microscopy of ferroelectric materials. *Appl Phys Lett* 88:062908.
45. Jesse S, et al. (2008) Direct imaging of the spatial and energy distribution of nucleation centers in ferroelectric materials. *Nat Mater* 7:209–215.
46. Ishibashi Y, Orihara H (1995) A theory of D–E hysteresis loop. *Integr Ferroelectr* 9:57–61.
47. Li W, Chen ZJ, Auciello O (2011) Calculation of frequency-dependent coercive field based on the investigation of intrinsic switching kinetics of strained $Pb(Zr_{0.2}Ti_{0.8})O_3$ thin films. *J Phys D Appl Phys* 44:105404.
48. Erni R, Rossell MD, Kisielowski C, Dahmen U (2009) Atomic-resolution imaging with a sub-50-pm electron probe. *Phys Rev Lett* 102:096101.